Electrochimica Acta 514 (2025) 145632

Contents lists available at ScienceDirect

Electrochimica Acta

journal homepage: www.journals.elsevier.com/electrochimica-acta

Tapered, interdigitated channels for uniform, low-pressure flow through porous electrodes for desalination and beyond

Md Habibur Rahman [a], Irwin C. Loud IV [a], Vu Q. Do [a], Md Abdul Hamid [a], Kyle C. Smith [a,b,c,d,*]

[a] Department of Mechanical Science and Engineering, Grainger College of Engineering, University of Illinois at Urbana-Champaign, Urbana, IL 61801, USA
[b] Department of Materials Science and Engineering, Grainger College of Engineering, University of Illinois at Urbana-Champaign, Urbana, IL 61801, USA
[c] Beckman Institute for Advanced Science and Technology, University of Illinois at Urbana-Champaign, Urbana, IL 61801, USA
[d] Computational Science and Engineering Program, Grainger College of Engineering, University of Illinois at Urbana-Champaign, Urbana, IL 61801, USA

ARTICLE INFO

Keywords:
Flow
Design
Electrochemistry
Desalination

ABSTRACT

Interdigitated flow fields (IDFFs) stand out among flow fields used in electrochemical energy storage and conversion for their modest pressure drop through electrodes. While recent efforts have sought to optimize flow-field topologies and channel shapes, we present a bottom-up strategy to taper channel cross-sections in IDFFs to maximize flow uniformity, eliminating the dead zones that plague straight channels. A linear variation in channel hydraulic conductance is shown to produce constant inter-channel velocity with minimal pressure drop, and mapping between conductance and cross-section geometry with appropriate Poiseuille flow relations enables their implementation. Using a micro-engraving process, we design and manufacture tapered channels having piecewise-constant cross-sections chosen from a library with different nominal widths and depths. The spacing between channels is then optimized to simultaneously minimize material removal and maximize apparent hydraulic permeability. Such tapered-channel IDFFs are embedded in porous, cation-intercalating electrodes for use in desalination by symmetric Faradaic deionization (FDI), where an increase in hydraulic permeability of tapered channels greater than two-fold compared to straight channels is shown to reduce pumping energy by 62% when desalinating seawater-salinity feeds. Energy efficiency doubles at 50% salt removal as a result, motivating hybridization of FDI with conventional desalination processes. Total energy consumption levels of 7.3 kWh/m^3 and 0.69 kWh/m^3 to produce freshwater respectively from seawater-salinity and brackish feeds is lower than small-scale reverse osmosis and thermal distillation. Low-pressure, high-efficiency operation enabled by IDFFs designed with optimally tapered channels motivates their broad use in flow-based electrochemical separations, energy storage, and energy conversion.

1. Introduction

Flow fields are indispensable for the low-pressure, high-rate operation of scalable electrochemical energy conversion and storage devices that use liquid or gaseous feeds, including fuel cells [1], flow batteries [2], and electrochemical separation devices [3–5]. Interdigitated flow fields (IDFFs) stand out among other flow fields due to their low pressure drop and facile electrochemistry achieved by forcing electrolyte flow through porous electrodes [6]. While serpentine flow fields have been shown to increase power density in flow batteries, pumping energy costs have been shown to be significant [7]. Direct comparison of mass transport limitations in interdigitated, serpentine, parallel, and spiral flow fields has also revealed the unique low-pressure capabilities of IDFFs due to the short flow paths between channels [8]. However, machine learning [9,10] and additive manufacturing techniques [11] have recently been used to explore flow-field design topologies that could further decrease pumping pressure. Iterative, physics-based design approaches have also been used to compensate for dead zones caused by fluid stagnation in electrode pores [12,13] by modifying channel depth locally [12]. Because the maximum current density i_{lim} that can be

* Corresponding author's address: 1206 W. Green St., Urbana, IL 61801
E-mail address: kcsmith@illinois.edu (K.C. Smith).

https://doi.org/10.1016/j.electacta.2024.145632
Received 16 November 2024; Received in revised form 19 December 2024; Accepted 31 December 2024
Available online 1 January 2025

sustained without depleting reactant is directly proportional to local superficial velocity u_s,[1] dead zones suppress the utilization of electrode active area so as to increase cell polarization. In addition, dead zones can trigger gas evolution reactions [14–16] that suppress reactant mass transfer [17]. While dead-zone compensated design can mobilize electrolyte, thus far such an approach has come at the cost of higher pumping power [12]. Other flow-field designs have mimicked biological networks, including hierarchical IDFFs [18,19] and lung-inspired flow fields [20] that improve mass transport and flow distribution. Here, we introduce a new bottom-up theory for the design of tapered channels within IDFFs to simultaneously mitigate dead zones and minimize pumping pressure. A subspace of infinitely many channel shapes is shown to uniformize flow in IDFFs, while linear scaling of hydraulic conductance is found to produce the smoothest conductance profile among all uniformizing channel shapes.

While recent efforts have systematically explored the arrangement of channels to create certain flow field topologies, efforts to maximize performance by making channel cross-sections vary along their length have employed impromptu designs to date, thus limiting the extension of such strategies broadly. To date, numerical and experimental studies on flow batteries and fuel cells have tapered IDFF channels linearly in their width [21–25], depth [26–31], or both [32] to minimize pressure drop. However, no past work to our knowledge has sought to uniformize flow in doing so, nor has past work considered other taper functions. It is the contention of the present work that the kinematics of fluid flow (i.e., the streamlines produced by the flow field) should inform the design of tapered channels. Our recent demonstration and quasi-1D theory of embedded, micro-interdigitated flow fields in intercalation-based Faradaic deionization [3] (FDI) support this contention. There, the flow uniformity produced by straight channels was shown to be affected by a single non-dimensional parameter Ξ that characterizes the ratio of the longitudinal hydraulic resistance within channels to hydraulic resistance within electrode material between channels [3]. Here, $\Xi \ll 1$ corresponds to small intra-channel hydraulic resistance that produces non-zero transverse velocity through porous electrode material, thus eliminating the formation of dead zones even when channels use a straight cross-section that is not tapered [3]. However, to satisfy such a condition requires a large channel width when electrodes are highly permeable, resulting in significant material removal that reduces electrode capacity when IDFFs are embedded in electrodes [3] rather than in abutting bipolar plates. Thus, IDFFs using straight channels are best suited for electrodes with low hydraulic permeability. We overcome this challenge by rationally varying channel cross-sections along the length of channels to eliminate dead zones, subject to the constraints of a micro-engraving process that we use to make them. We do this by leveraging a quasi-1D theory of flow to inform the tapering of IDFF channels based on linear scaling of hydraulic conductance along each channel's length. In turn, we quantify the impact of such tapered IDFFs on the desalination performance achieved in intercalative FDI, where past research [4,33] apart from our own has used flow-by configurations that suffer from pervasive electrolyte stagnation.

In this work, we present a rational design strategy for the uniformization of flow by tapering the channels used in IDFFs. We embed such tapered, interdigitated channels within porous electrodes incorporating nickel hexacyanoferrate for use in intercalative Faradaic deionization. The tailoring of channel cross-sections is first deduced from an analysis of the resulting flow through the electrodes based on quasi-1D theory. A conductance library is then generated by micro-engraving straight channels with different channel widths and depths into porous electrode material. Tapered IDFF channels with linear scaling of channel conductance are then achieved by varying cross-sections in a piecewise-constant fashion. The inter-channel spacing between tapered IDFF channels is also determined to minimize material removal while maximizing electrode hydraulic permeability, which is shown to exhibit a percolative dependence on flow-path length. The electrodes embedded with optimally tapered IDFF channels are then used in a symmetric FDI flow cell to desalinate feeds with brackish and seawater salinity.

[1] The steady-state limiting current density for one-dimensional flow is given as: $i_{lim} = u_s C_{in} F(h/s)$, where C_{in} is the feed concentration of reactant, F is Faraday's constant, h is electrode thickness, and s is flow-path length. This formula is derived in Section 1 of the Supporting Information.

2. Results and discussion

2.1. Theory of optimal tapering to uniformize flow

We used quasi-1D theory [3] to analyze the flow through IDFFs using either straight or optimally tapered channels, the results of which are shown in Fig. 1 and the derivations of which are shown in Section 2 of the Supporting Information (SI). Subsequently, we also describe salient features of the approach used to deduce the design principles for optimal tapering of channels. We show that optimal tapering is achieved by using cross-section variations that produce a certain functional variation of the hydraulic conductance G, which is defined for Poiseuille flow as $G \equiv -\dot{V}\mu/(dp/dx)$ with $\dot{V}$ being the volumetric flow rate, μ being the dynamic viscosity, and dp/dx being the longitudinal pressure gradient. For laminar, fully developed flow through a rectangular channel cross-section having depth h that is much greater than its width w, hydraulic conductance is shown to follow a local-cubic law [34]: $G = hw^3/12$. In general, the conductance obtained for laminar, fully developed flow depends on geometry alone, consistent with its unit of m^4. Also, the conductance produced by arbitrarily shaped channel cross-sections can be predicted numerically, as we demonstrate later for trapezoidal cross-sections produced by V-bit engraving.

The results of our quasi-1D analysis of IDFF flows produced using either straight or optimally tapered channels are shown in Fig. 1 and Table S1. Straight channels used in IDFFs possess channel conductance that remains constant along each channel (Fig. 1 a), whereas optimally tapered channels possess a linear variation of hydraulic conductance (Fig. 1 f). We note that such linear variation of hydraulic conductance does not necessarily dictate linear variation of any individual cross-sectional parameter. For a rectangular cross-section whose width w is varied while its depth h is fixed and where $h \gg w$ is satisfied, linear conductance scaling dictates that channel width varies with the cubic-root of longitudinal position x (see Fig. 1 f inset): $w = w_0(1 - x/L)^{1/3}$, where w_0 is maximal channel width and L is channel length. Ultimately, the conductance variations that a given channel shape possesses are shown to produce a certain transverse velocity distribution between high- and low-pressure channels through porous electrode material. For IDFFs using straight channels transverse superficial velocity $u_{s,\perp}$ deviates from uniformity to an increasing degree when channel length is increased *ceteris paribus* (Fig. 1 e). In contrast, for IDFFs that use optimally tapered channels transverse velocity is uniform irrespective of channel length (Fig. 1 j), provided that the spacing between channels is large enough that the span of intervening porous electrode material varies weakly among all flow paths. Sufficient separation between channels is required because we assume an invariant flow-path length to deduce that linear conductance scaling produces uniform flow, as shown later.

The variation of longitudinal flow rate $\dot{V}_{\parallel}(x)$ within high- and low-pressure channels determines their respective pressure distributions $p^H(x)$ and $p^L(x)$, which in turn produce the inter-channel pressure difference $\Delta p(x) = p^H(x) - p^L(x)$ that drives transverse velocity $u_{s,\perp}$ through porous electrode material. For IDFFs using straight channels longitudinal volumetric flow rate varies in a non-linear fashion (Fig. 1 b) to produce channel pressure distributions with an exponential-like decay (Fig. 1 c). The difference in slope between $p^H(x)$ and $p^L(x)$ at a given position results in the inter-channel pressure difference being non-

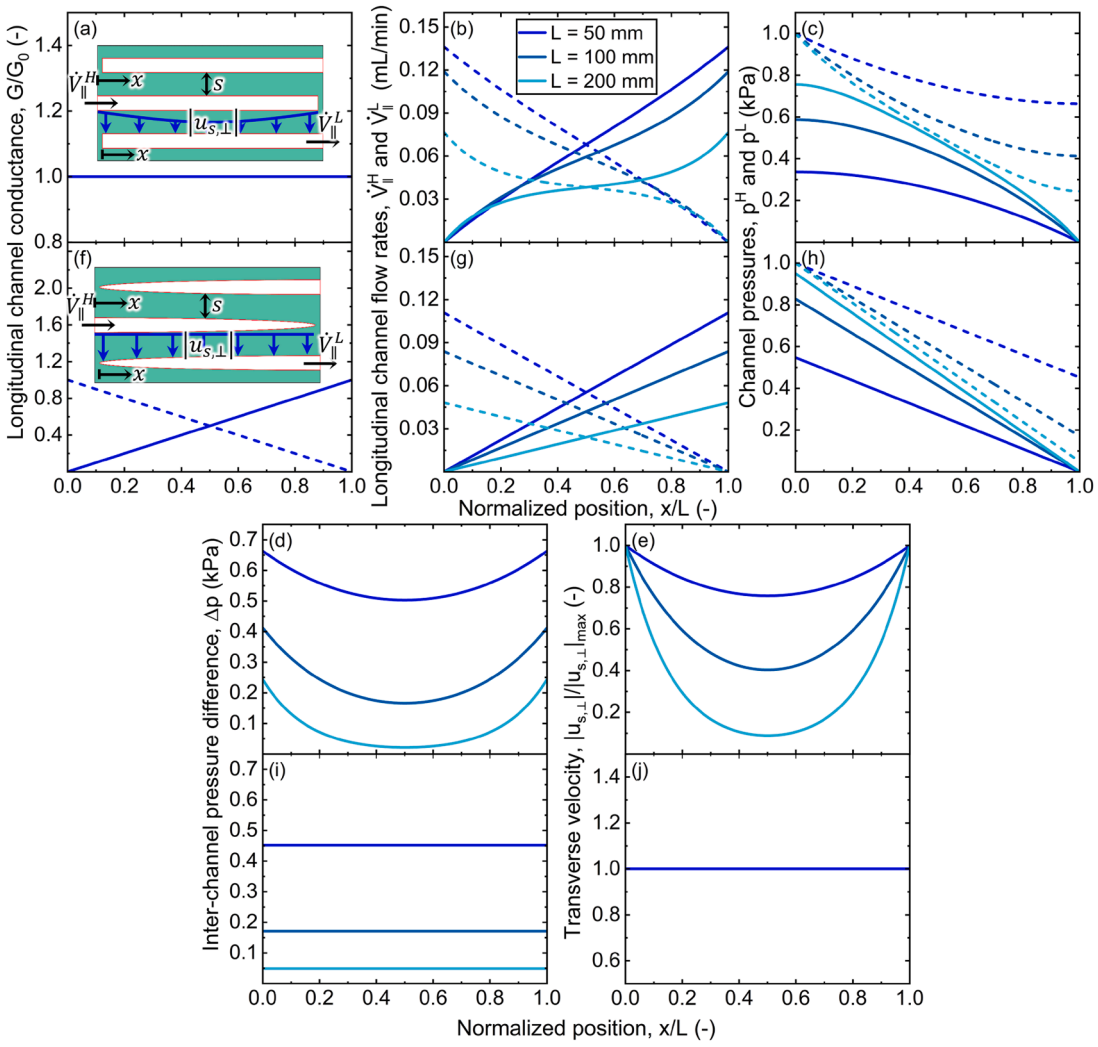

Fig. 1. Longitudinal distributions of channel hydraulic conductance (a,f), longitudinal channel flow rate (b,g), channel pressure (c,h), inter-channel pressure difference (d,i), and transverse superficial velocity (e,j) for IDFFs using straight (a-e) and tapered (f-j) channels with length L. Figs. 1b-c,f-h use dashed and straight lines respectively for high- and low-pressure channel distributions.

uniform (Fig. 1 d). In contrast, for IDFFs using optimally tapered channels longitudinal flow rate varies linearly (Fig. 1 g) to produce a linear variation of pressure in each channel. Because $p^H(x)$ and $p^L(x)$ possess identical slopes inter-channel pressure difference becomes uniform (Fig. 1 i). We also note that though the total supply pressure (i.e., $p^H(x=0) - p^L(x=L)$) needed for IDFFs using either straight or tapered channels is the same (Fig. 1 c,h), straight channels produce a higher total flow rate (Fig. 1 b) than tapered ones (Fig. 1 g) when both types of channels use the same maximal cross-section. However, tapered-channel IDFFs possess a smaller volume than straight-channel IDFFs due to a corresponding straight channel's profile circumscribing that of a tapered channel. In practice, we show later that when channel volume fraction is fixed among straight- and tapered-channel IDFFs, tapered-channel IDFFs produce higher apparent permeability. Next, we describe the theory used to deduce that linear conductance scaling produces uniform flow.

Our novel tapering approach for IDFFs based on the linear scaling of channel hydraulic conductance is dictated by the condition that the transverse superficial velocity $u_{s,\perp}$ between high- and low-pressure channels is invariant along such channels. By subjecting the quasi-1D equations that model flow distribution through IDFFs to a uniform $u_{s,\perp}$ condition, we prove that interdigitated channels that possess linear scaling of hydraulic conductance (Eq. 4; [35]) *uniquely* satisfy this constraint with the smallest mean-square slope. We then explain how such hydraulic conductance variations can be produced by a variety of means, depending on the specific channel cross-section and variation thereof that is sought.

We now determine design formulas for the tapering of channel cross-sections to produce uniform transverse velocity between high- and low-pressure channels [35]. Readers with interest in using the theory are directed to Eqs. 2-4 for conductance profiles that uniformize flow. The approach used produces certain tapers that are similar to the tapered headers used for manifolds with uniform flow [36,37]. For simplicity we assume that the inter-channel distance $s(x)$ is a weak function of x such that we approximate it using a constant value s_r that is representative over the entire range of x: $s(x) \approx s_r$. Application of Darcy's law subject to uniform $u_{s,\perp}$ implies that the pressure difference Δp between high- and low-pressure channels is invariant along these channels:

$$\Delta p = p^H - p^L = \frac{|u_{s,\perp}|\mu s_r}{k_{pe}}$$

where $p^H(x)$ and $p^L(x)$ respectively capture the pressure variations with longitudinal position x within high- and low-pressure channels. k_{pe} and μ respectively are the hydraulic permeability of the porous electrode and the dynamic viscosity of the working fluid. The quasi-1D theory also couples the variations of pressure within each channel to the hydraulic conductance variations that we seek to optimize: $G^H(x)$ and $G^L(x)$. In

general, these effects are captured using the following differential equations that enforce the conservation of volumetric flow rate within each channel, as described in SI Sec. 2:

$$\frac{d}{dx}\left[\frac{G^H}{\mu}\frac{dp^H}{dx}\right] + 2h|u_{s,\perp}| = 0$$

$$\frac{d}{dx}\left[\frac{G^L}{\mu}\frac{dp^L}{dx}\right] - 2h|u_{s,\perp}| = 0$$

We now enforce $|u_{s,\perp}|$ to be invariant with x, allowing the above equations to be integrated directly to yield explicit functions of x for the longitudinal flow rates $\dot{V}_{\parallel}^{H}(x)$ and $\dot{V}_{\parallel}^{L}(x)$:

$$\dot{V}_{\parallel}^{H}(x) = -\frac{G^H}{\mu}\frac{dp^H}{dx} = -\int 2h|u_{s,\perp}|dx = -2h|u_{s,\perp}|x + \kappa_H$$

$$\dot{V}_{\parallel}^{L}(x) = -\frac{G^L}{\mu}\frac{dp^L}{dx} = \int 2h|u_{s,\perp}|dx = 2h|u_{s,\perp}|x + \kappa_L$$

By neglecting flow through the tip of both channels (i.e., $\dot{V}_{\parallel}^{H}(x=L) = 0$ and $\dot{V}_{\parallel}^{L}(x=0) = 0$), we find the integration constants κ_H and κ_L:

$$\dot{V}_{\parallel}^{H}(x) = -\frac{G^H}{\mu}\frac{dp^H}{dx} = 2hL|u_{s,\perp}|(1 - x/L)$$

$$\dot{V}_{\parallel}^{L}(x) = -\frac{G^L}{\mu}\frac{dp^L}{dx} = 2hL|u_{s,\perp}|(x/L)$$

Consistent with our enforcement of uniform transverse velocity, which in turn requires that Δp is invariant along channels, the gradient of Δp must therefore be zero:

$$\frac{d(\Delta p)}{dx} = \frac{dp^H}{dx} - \frac{dp^L}{dx} = 0$$

Utilizing the preceding expressions for $\dot{V}_{\parallel}^{H}(x)$ and $\dot{V}_{\parallel}^{L}(x)$, we obtain a relation that governs the conductance distributions $G^H(x)$ and $G^L(x)$ within the respective channels:

$$\frac{1 - x/L}{G^H(x)} - \frac{x/L}{G^L(x)} = 0$$

We opt to taper high- and low-pressure channels in the same manner such that their conductance distributions are anti-symmetric: $G^L(L - x) = G^H(x)$. Consequently, we obtain a *functional equation* that constrains the high-pressure channel's conductance distribution:

$$G^H(x)\cdot x = G^H(L - x)\cdot(L - x) \tag{1}$$

In actuality, Eq. 1 defines a space that includes infinitely many conductance profiles. A necessary and sufficient condition to satisfy this equation is that $f(x') = (L/2 \pm x')\cdot G^H(L/2 \pm x')$ be an even function, where $x' = x - L/2$. Thus, a conductance profile that uniformizes flow can be generated by using any trial profile $g(x)$:

$$G^H(x) = \frac{x\cdot g(x) + (L - x)\cdot g(L - x)}{2x} = \frac{g(x) - g(L - x)}{2} + \frac{g(L - x)}{2(x/L)} \tag{2}$$

While the above conductance profile may be singular for vanishing x, in Section 3 of the SI we show that the following cosine series forms a subspace of profiles that satisfy Eq. 1 without discontinuities or singularities:

$$G^H(x) = \frac{1}{x}\sum_{n=1}^{\infty} b_n\left[\cos\left(\frac{n\pi}{L}\left(x - \frac{L}{2}\right)\right) - \cos\left(\frac{n\pi}{2}\right)\right] \tag{3}$$

where the coefficients b_n can be chosen arbitrarily. Using Eq. 2 one can show that a linear conductance profile is the lowest-order polynomial profile that uniformizes flow between channels. Further, when negligible flow occurs through channel tips the following linear conductance profile is obtained:

$$G^H(x) = G_0\cdot(1 - x/L) \tag{4}$$

where G_0 is the high-pressure channel's conductance at its inlet. This linear profile is readily shown to minimize the mean-square slope of conductance $\left\langle \left(dG^H/dx\right)^2 \right\rangle$:

$$\left\langle \left(dG^H/dx\right)^2 \right\rangle = \left\langle dG^H/dx \right\rangle^2 + \left\langle \left\langle dG^H/dx \right\rangle - dG^H/dx \right\rangle^2$$

where $\langle f \rangle = \int (f/L)dx$ is an integral average operator. Since dG^H/dx is constant for a linear conductance profile, it has no fluctuation from its mean, resulting in all other profiles with the same mean slope having greater mean-square slope.

We also observe that other conductance profiles that satisfy the uniform flow condition generally produce larger pressure drops than the linear profile. To show this, we systematically perturbed the conductance profile of Eq. 4 from linearity, while constraining channel volume and flow rate to be the same among all taper-channel IDFFs, by adjusting the coefficients of its cosine-series expansion:

$$G^H(x) = G_0\left(1 - \frac{x}{L}\right) = G_0\frac{L}{x}\sum_{n=1}^{\infty}\frac{4(-1)^{n+1}}{n^2\pi^2}\left[\cos\left(\frac{n\pi}{L}\left(x - \frac{L}{2}\right)\right) - \cos\left(\frac{n\pi}{2}\right)\right]$$

Figure S2 shows that the pressure drop produced with linear conductance scaling is within 0.2% of all perturbed profiles, demonstrating the unique ability of linear conductance scaling to enable low-pressure flow.

In what follows we exclusively use the above linear channel conductance profile. The tapering profile can be determined using the correlation between the local hydraulic conductance and the desired channel cross-section. For example, one can vary the width of the channel while keeping the depth fixed, which results in a cubic-root tapering profile in the width if $w \ll h$ or a linear tapering in the width if $w \gg h$ [36,38]. Similar results can be achieved if the depth is varied and the width is fixed. However, variation in either the width or the depth could lead to feature sizes that are not resolvable by a given manufacturing method, as discussed later. Therefore, to manufacture tapered channels in this work we varied both their depth and width to achieve maximal channel resolution.

2.2. Design for manufacturability and maximal permeability

We created an experimental library of channel cross-sections determined by optical profilometry to correlate hydraulic conductance G with specific micro-engraving conditions (Fig. 2 a,c). The porous, intercalative electrodes in which channels were embedded are used later in desalination by symmetric Faradaic deionization. This library was used to design tapered channels having piecewise-constant cross-sections to approximate a linear conductance variation that is sought to uniformize flow (Fig. 2 b). Laser micro-machining was also prototyped using similar approaches (SI Sec. 13), demonstrating the versatility of our approach. Precision engraving with a V-shaped cutting tool was used to create channels with widths ranging from 150 to 450 μm and depths ranging from 75 to 200 μm using a desktop CNC machine (Fig. 2 a,c). Simulated axial velocity distributions resulting from laminar, fully developed Poiseuille flow show that flow in most instances is two-dimensional (Fig. 2 a), justifying our numerical determination of G rather than estimating it with the local-cubic law. To determine the specific piecewise-constant cross-section variation used to uniformize flow, the set of conductance values obtained by varying width and depth jointly were overlaid as segments onto an ideal theoretical curve (Fig. 2 b). Joint variations of width and depth were used because varying either of the two dimensions separately while fixing the other either produced

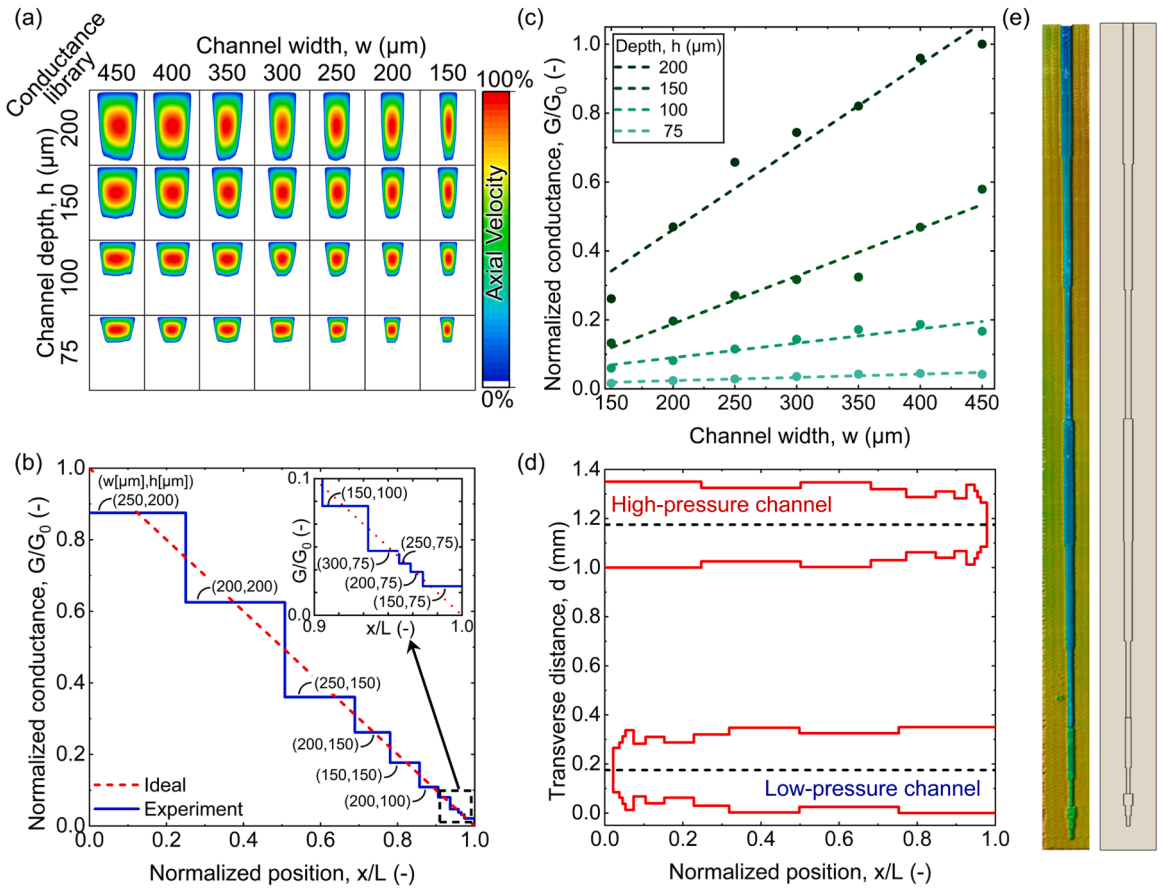

Fig. 2. (a) Conductance library with distinct width and depth combinations, showing axial velocity distributions for each channel cross-section. (b) Theoretical and experimental conductance variation along a tapered channel with piecewise-constant cross-sections. (c) Channel conductance as a function of channel width and depth. (d) Width variations of high- and low-pressure channels. (e) Optical profilometry of a representative tapered channel compared with that of the felicitous design.

~10% unresolved channel length or a first segment length approaching 50% of the channel's entire length (Section S4 in the SI). The length for the segment having maximal conductance was first chosen to make that segment's center intersect the ideal curve (Fig. 2 b). For all other segments an 'anchor point' was chosen based on the position at which each segment's conductance coincided with the ideal curve. The right end point of the interval for each segment was then assumed to equal half the distance between anchor points to the left and right. This strategy approximates the ideal curve to approach a midpoint rule, which produces second-order accuracy for integration. The resulting variations of nominal width, depth, and length for each channel segment are shown to vary non-monotonically along each channel (Table S2; Fig. 2 b), as verified using optical profilometry (Fig. 2 d,e).

Tapered channels designed using the aforementioned strategy were used to create IDFFs milled onto 45 mm × 45 mm electrodes. In addition to the tapered profile already described, the interdigitation of channels requires the specification of their center-to-center spacing s_{cc} and a gap distance g between channel tips and electrode edges. In practice, we made IDFFs with s_{cc} equal to 900 μm and 3.2 mm to probe the impact of spacing on apparent permeability and electrode capacity, as discussed later. A finite, non-zero gap distance is also needed to suppress direct flow between the tip of each channel and its adjacent electrode edge, the effect of which was assumed negligible when deriving the associated conductance scaling formula for uniformizing flow. Conversely, too large of a gap produces dead zones at channel tips. Our analysis of this effect in Sec. S5 of the SI yields a formula for the minimum gap distance to suppress tip flow to <1% for electrodes with isotropic permeability: $g > 50 w_0 s_r / L$, where w_0 and L are the maximal width and length of the channel and s_r is the representative inter-channel distance. For the IDFF using s_{cc} equal to 900 μm the minimum gap distance was 214 μm. A gap distance equal to 500 μm was targeted to produce 44.5 mm long channels, but ~1 mm was engraved in practice due to the finite resolution of our engraving technique.

To quantify the impact of s_{cc} on the local permeability of unpatterned electrode material, four electrodes were engraved with parallel channels extending along the entire length of each electrode, each using different inter-channel spacing (Table S5). Hydraulic permeability was then measured with the associated channels oriented perpendicular to the flow direction, rather than parallel to it, to systematically vary the contiguous flow path lengths through porous electrode material (Fig. 3 a). Unexpectedly, the measured hydraulic permeability was shown to increase from practically zero for inter-channel distance $s > 1.5$ mm toward an upper bound of 0.5 μm^2 for $s < 0.5$ mm according to a $\approx 1/5^{\text{th}}$ power law in the deviation from the threshold flow-path length s_c (Fig. 3 a). Such scaling is evidence of liquid-phase percolation within the pores of the electrodes that also raises questions concerning the wettability of our electrodes. One contributing factor is the hydrophobic nature of the polyvinylidene fluoride (PVdF) binder [39,40] used in our electrodes, which could inhibit water from infiltrating micropores. Predicated on the possibility of such a mechanism, the apparent hydraulic permeability of an electrode engraved with parallel channels was measured using both air and water as working fluids with an orientation parallel to the flow direction rather than perpendicular to it (Fig. S5). While water produced a permeability of only 140 μm^2, air produced a permeability of 240 μm^2 which is in much better agreement with the calculated theoretical hydraulic permeability of 270 μm^2 (Table S6). Hence, we

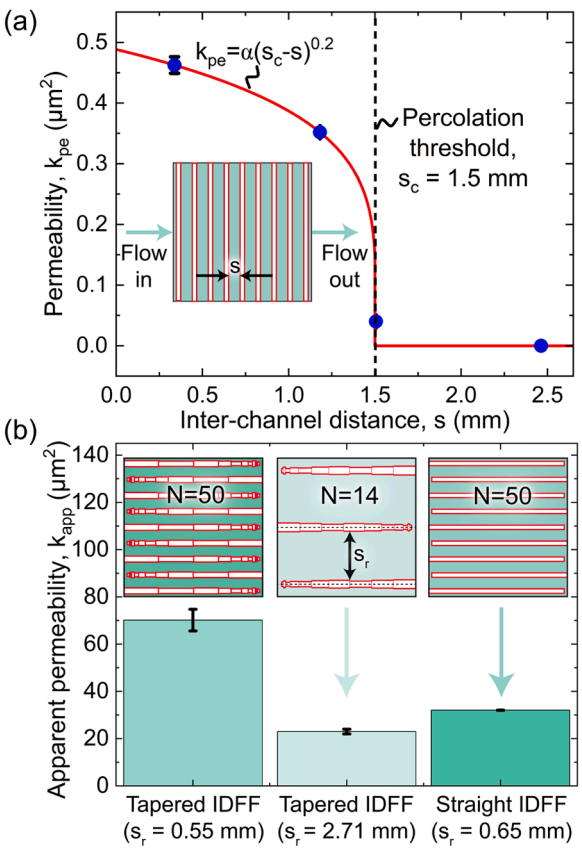

Fig. 3. (a) Local, unpatterned electrode permeability as a function of inter-channel distance measured from experiments using thru-channels oriented perpendicular to flow. (b) Apparent permeability of patterned electrodes using tapered-channel and straight-channel IDFFs with different representative inter-channel distance s_r.

conclude that the percolative dependence of hydraulic permeability on flow-path length is linked to the presence of trapped air within certain pores. Despite this implication the wettability of V-bit engraved electrode surfaces is shown to be better than laser-micromachined surfaces (Fig. S20), motivating deeper investigation of electrode wetting.

We used the associated knowledge of flow-path length dependent hydraulic permeability to design tapered-channel IDFFs that maximize apparent permeability. We created such IDFFs using inter-channel distances below (s = 550 μm) and above (s = 2.7 mm) the percolation threshold. Despite the electrode with larger inter-channel distance using bigger channels (w_0 = 510 μm) than the other (w_0 = 350 μm), the electrode having smaller channels produced more than three-fold larger apparent permeability (Fig. 3 b). This increase in permeability is attributable at least in part to a shorter flow-path length resulting in greater local, unpatterned electrode permeability (cf. Fig. 3 a). Additionally, the electrode having smaller tapered channels and shorter inter-channel distance produced more than two-fold larger apparent permeability than an electrode patterned with a straight-channel IDFF having similar material removal and inter-channel distance. This increase in permeability can be attributed to the tapering of IDFF channels that also minimizes the effect of dead zones to which straight-channel IDFFs are susceptible [3].

2.3. Desalination using symmetric, intercalative FDI

Desalination experiments were carried out with tapered-channel IDFFs embedded in nickel hexacyanoferrate (NiHCF) cation intercalation electrodes using the in-house symmetric Faradaic deionization (FDI) apparatus depicted in Figs. 4 a,b. While we previously used a heated, alkaline-pH coagulation bath in wet-phase inversion to solidify electrodes after slurry casting [3,41], here we used a heated, neutral-pH coagulation bath to eliminate PVdF dehydrofluorination at pH > 11 (see SI Sec. 9). Constant heating of a neutral-pH bath also produced higher electronic conductivity than with transient heating (Fig. S8), while producing 20% higher first-cycle charge efficiency than with heated, alkaline wet-phase inversion (Fig. S9). During each desalination half-cycle, one such electrode intercalates Na^+ ions to produce diluate, while the other electrode deintercalates Na^+ ions to produce brine (Fig. 4 a,c). In turn, Cl^- ions transfer through an intervening anion-exchange membrane (AEM) to compensate for charge balance [42]. As in our earlier work [3,41], we recirculate diluate and brine between reservoirs and electrodes at a constant flow rate of 5 mL/min to minimize the state-of-charge gradients resulting from streamwise concentration polarization [43,44]. The finite specific capacity for cation (de)intercalation within electrodes dictates the use of valve switching to redirect diluate and brine to opposing electrodes when current is switched. While this approach bears similarity with electrodialysis reversal that is used to mitigate fouling and scale formation [45], such current switching is necessary in symmetric, intercalative FDI to make desalination pseudo-continuous [41], unless device architecture is modified to eliminate solution switching [46]. The apparent mixing between diluate and brine streams is inevitable to valve switching, but here we minimize its effect by introducing a calibrated delay of 3.2 s between the switching of inlet and outlet valves following Ref. [41] (Fig. S6c).

Fig. 4 c shows the resulting variations of current, cell potential, and salt concentration for a representative experiment. Cell potential varies between -0.4 V and 0.4 V among galvanostatic charge and discharge half-cycles with 1 mA/cm^2 current. Such variations of cell potential V and current I produce the electrical contributions to energy consumption: $E_{elec} = \int I{\cdot}V dt$. Pumping energy consumption $E_{pump} = \int p_{supply}{\cdot}\dot{V}_{total} dt$ results from the supply pressure $p_{supply} = \dot{V}_{total} L_{e,\|} \mu / \left(k_{app} L_{e,\perp} h\right)$ needed to force water at a total flow rate $\dot{V}_{total}$ through IDFF-patterned electrodes having certain apparent permeability k_{app}. Here, $L_{e,\|}$ and $L_{e,\perp}$ are respectively the longitudinal and transverse dimensions of the electrode. After each half-cycle there is a sudden change in concentration that is evidence of inter-stream mixing (Fig. 4 c). This effect becomes more prominent with increasing concentration difference between the diluate and brine reservoirs, ultimately reaching a limiting point where the deleterious concentration change due to mixing matches the beneficial concentration change caused by the applied current [3]. We also note that concentration increase within the brine reservoir is suppressed due to an extent of water crossover through the AEM [3].

Fig. 5 shows the volumetric energy consumption (VEC) and thermodynamic energy efficiency for desalination experiments including pumping energy alone E_{pump}, including electrical energy alone E_{elec}, and total energy E_{total} including electrical and pumping energies. Each experiment was conducted in triplicate with the values shown being the average among all experiments, while error bars indicate their standard deviation. Fig. 5 a-c show the desalination performance of electrodes using tapered-channel IDFFs with seawater-level salinity feed (510 mM NaCl), as compared to those of straight-channel IDFFs. Tapered- and straight-channel IDFFs are shown to produce salinity near that of freshwater (17 mM) with 19 mM and 14 mM, respectively (Fig. 5 c). Fig. 5 a shows that a 62% reduction in VEC due to pumping energy is achieved with tapered-channel IDFF electrodes (2.5 kWh/m^3) as compared to straight-channel electrodes (6.6 kWh/m^3) at maximal salt removal. The energy saved by using electrodes with tapered-channel IDFFs is caused by their 2-3 times increased apparent permeability. Including both electrical and pumping energy consumption, the VEC at maximal salt removal of tapered-channel IDFFs (7.3 kWh/m^3) is 32% lower compared to straight-channel IDFFs (11 kWh/m^3). Both types of IDFF channels show superior total VEC relative to small-scale seawater

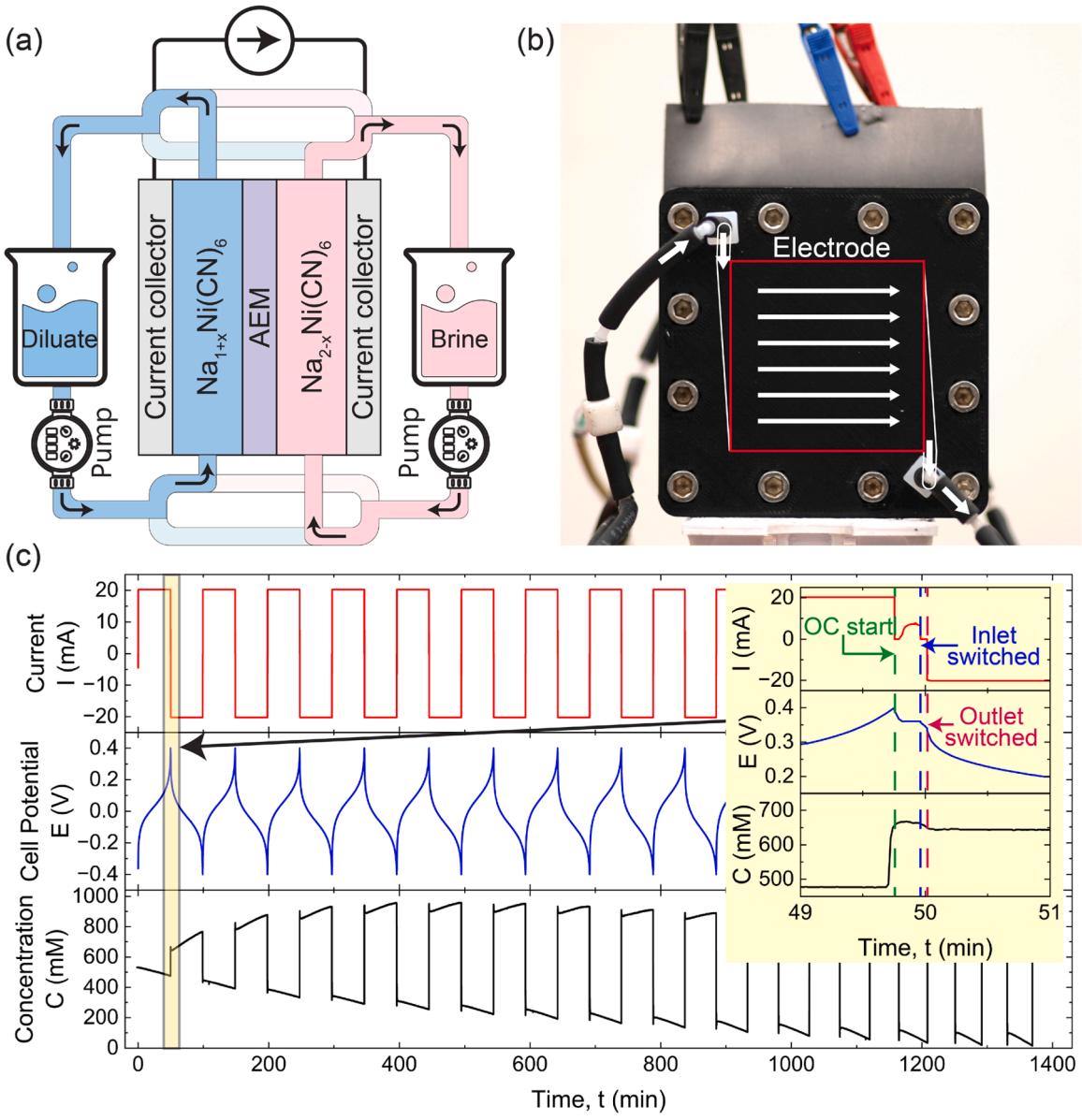

Fig. 4. (a) Layout of the symmetric FDI flow cell incorporating NiHCF electrodes patterned with tapered-channel IDFFs through which diluate and brine feeds are recirculated. (b) Side view of the FDI cell showing flow from inlet to outlet. (c) Time variations of applied current, cell potential, and salt concentration during consecutive charge-discharge cycles for desalination with 510 mM NaCl influent using taper-channel IDFFs embedded with 350 μm maximal width. The inset shows the start of open-circuit (OC) conditions and the switching of inlet and outlet valves that occurs at the end of each half-cycle.

reverse osmosis (RO; 15 kWh/m^3), multistage flash distillation (20-27 kWh/m^3), multi-effect distillation (14-21 kWh/m^3), and thermal vapor compression (16 kWh/m^3) [47].

The thermodynamic energy efficiency of tapered-channel IDFFs is shown to be substantially greater than that of straight-channel IDFFs when desalinating feeds with seawater-level salinity (Fig. 5 b). While only a 1.3-fold improvement in efficiency is shown at maximal salt removal, at ≈50% salt removal tapered-channel IDFFs double the total thermodynamic energy efficiency including electrical and pumping energy (18%) relative to straight-channel IDFFs. While 50% salt removal may be impractical if standalone FDI is used for desalination, applications using conventional desalination processes could use this FDI process for pre-treatment when the feed concentration of source water exceeds the rated concentration (e.g., in littoral waters). While tapered-channel IDFFs present promising thermodynamic energy efficiency, the gap between its value including electrical energy alone and total energy indicates that further improvements in hydraulic permeability could produce total energy efficiency as high as 38% at ≈50% salt removal and as high as 13% at maximal salt removal.

Fig. 5 d-e show the results of desalination experiments using tapered-channel IDFFs fed with brackish water containing 104 mM NaCl. Here, only 0.19 kWh/m^3 of pumping energy was needed to produce 8 mM salinity below freshwater compared to 2.5 kWh/m^3 for desalination of seawater salinity. Including pumping losses the total energy consumption of only 0.69 kWh/m^3 is still lower than that of brackish water RO (1.5-2.5 kWh/m^3) and electrodialysis (2.6-5.5 kWh/m^3) [47]. Furthermore, these tapered-channel electrodes obtain a maximum thermodynamic energy efficiency of 31% with 82% salt removal, outperforming RO [48], electrodialysis [48], and capacitive deionization using electric double layers [49].

The specific energy consumption (SEC) resulting from tapered-channel IDFF experiments was also compared with that of earlier FDI work that used symmetric Prussian blue analogue electrodes. In contrast with our own work that achieves high salt removal from high-salinity

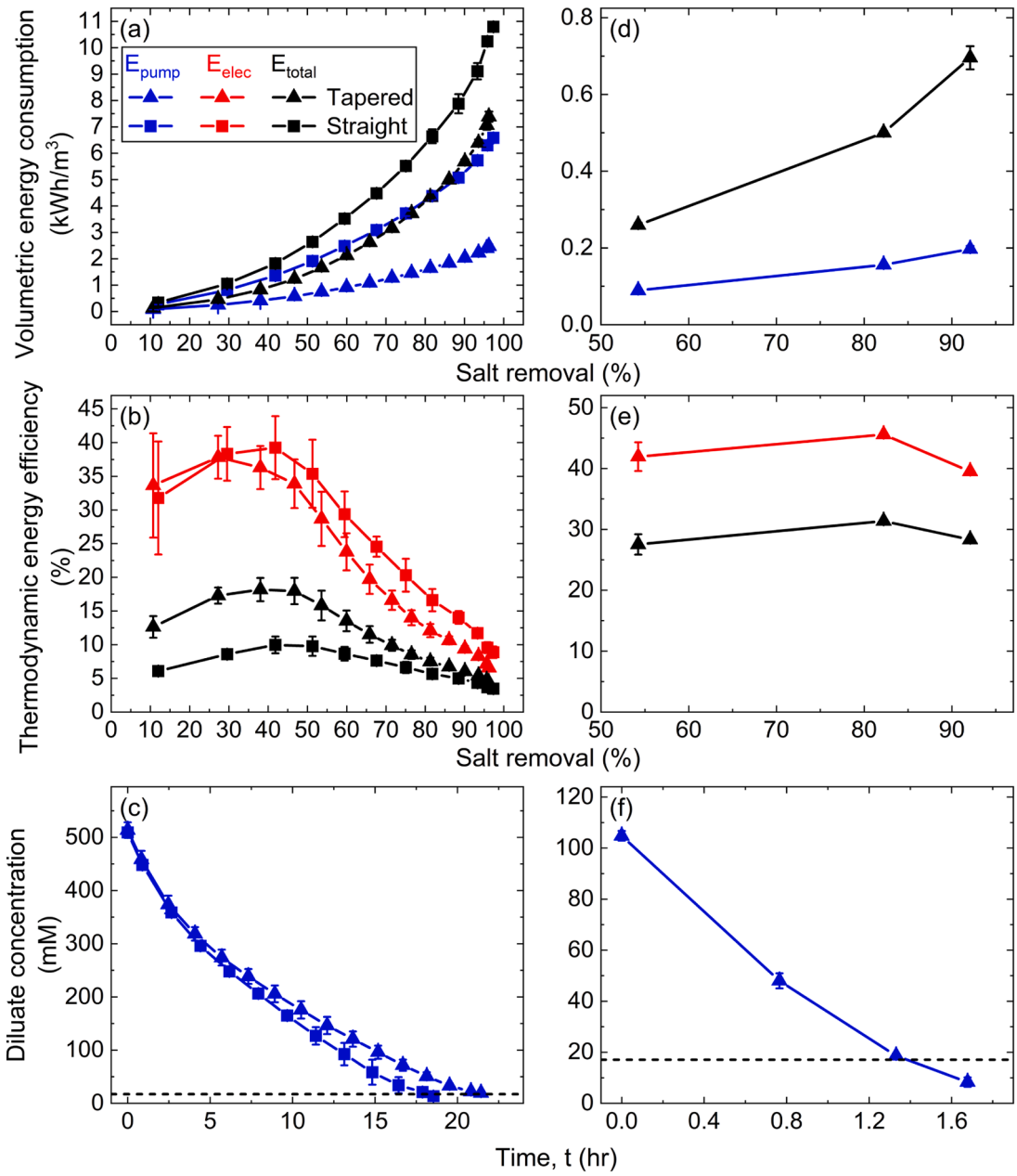

Fig. 5. Desalination performance of tapered- and straight-channel IDFFs using feeds with (a-c) seawater-level salinity (510 mM NaCl) and (d-f) brackish salinity (104 mM NaCl) in terms of (a,d) volumetric energy consumption, (b,e) thermodynamic energy efficiency, and (c,f) diluate concentration.

feeds, Fig. 6 shows that other work aside from our recent work [3,41] either has desalinated brackish feeds with modest salt removal less than 60% [50–54] or has desalinated feeds with seawater-level salinity with even lower salt removal of 20% [55]. However, the batch-type experiments that we perform produces a range of SEC values resulting from the increasing degree of salt removal with increasing number of electrochemical half-cycles (see Fig. 5). Our experiments performed using brackish feeds with 50% salt removal produced similar electrical SEC contributions to earlier experiments [50–52] with less than 30% salt removal. Our experiments performed using seawater-salinity feeds with 10% salt removal produced half the electrical SEC of earlier experiments with 20% salt removal [55]. In addition, the present tapered-channel desalination experiments performed using seawater-level salinity with salt removal >95% show a 30% reduction in total SEC from our previous work that used straight-channel IDFFs [3].

In addition to the low energy consumption needed when using tapered-channel IDFFs, their decreased supply pressure reduces the driving force for water crossover through AEMs, as quantified by process water recovery and charge efficiency. Water recovery [49] is defined as the ratio of the diluate volume V_D to the total water volume V_{total}: $WR = V_D/V_{total}$. Charge efficiency [56] Λ is defined as the ratio of the moles of salt removed n_{salt} to the moles Q/F of charge Q transferred. For seawater-salinity feed, both water recovery and charge efficiency decrease from their initial half-cycle values by more than half (Fig. S7). However, tapered-channel IDFFs show only very weak drops in both water recovery and charge efficiency for brackish-salinity feeds. The apparent water crossover rates through the AEM were measured as 0.11 L/m^2-h and 0.091 L/m^2-h respectively with seawater and brackish salinity feeds. These rates are lower than those reported for commercially available membranes [57], electrodialysis [58], and flow batteries [59], which typically range from 0.24-2.5 L/m^2-h.

Despite these promising results, a limitation of the current symmetric FDI process is its water production rate of 0.077 L/m^2-h in seawater and 2.3 L/m^2-h in brackish water desalination, which is lower than that of

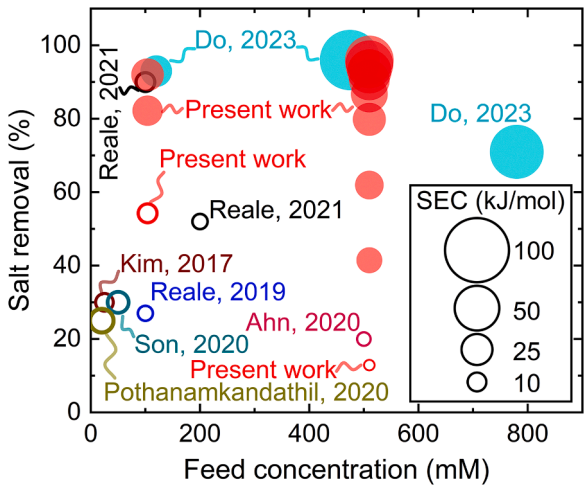

Fig. 6. Specific energy consumption (SEC) as a function of salt removal and feed concentration obtained using tapered-channel IDFFs, as compared with previous studies using Faradaic deionization (FDI) with symmetric Prussian blue analogue electrodes. Bubble area corresponds to SEC [3,41,50–53,55]. Data shown with unfilled circles include only electrical energy contributions to SEC, whereas the remaining data include both electrical and pumping energy contributions.

electrodialysis (~10 L/m^2-h) [60,61], motivating further research. While channel design does not directly influence water productivity, it enables a scaled-up system to perform more efficiently. To achieve a nominal water productivity of 1 L/h with the present seawater desalination productivity of 0.077 L/m^2-h, the present architecture would need 13 m^2 of membrane area. Such an area could be achieved by either increasing electrode size or by using a stack of multiple electrode pairs. However, an increase in electrode size inherently demands longer channel lengths. Our proposed tapered-channel IDFFs ensure that transverse superficial velocity remains uniform irrespective of channel length (see Fig. 1 j). Increased current density can be used to increase productivity in conjunction with increased electrode area, albeit with increased electrical energy consumption. Patterning of tapered-channel IDFFs on large-format electrodes must also be addressed to scale up productivity. The present method of direct milling presents a bottleneck due to the fine features of tapered channels. Here, the milling of tapered-channel IDFF electrodes with an area of only 20 cm^2 required 6.5 hours. Given that milling time scales linearly with area, alternative high-throughput patterning techniques such as laser engraving are imperative to scaling up the patterning of tapered-channel IDFFs.

3. Conclusions

We have introduced a novel design strategy for the tapering of channels used in IDFFs to eliminate the dead zones to which straight channels are prone, culminating in their experimental implementation for IDFFs embedded in cation intercalation electrodes for electrochemical desalination. In addition to electrochemical separations, channel tapering of this sort can be applied broadly to facilitate the flow of liquid electrolyte or of gaseous feeds in flow batteries and fuel cells that use IDFFs machined into bipolar plates. Our approach based on a quasi-1D theory of flow yields a simple design formula that forces the hydraulic conductance along channels to vary linearly. This design formula is unique among other conductance profiles that satisfy the uniform flow condition (Eq. 1) in that it minimizes pressure drop and mean-square slope. It is possible that for certain applications other objective functions could be of interest for minimization, in which case the subspace of conductance profiles can be explored using an infinite cosine series (Eq. 3) or using trial conductance profiles (Eq. 2). Our approach can be extended more broadly by also including the effect of non-uniform flow-path length between channels, though we approximate it as a constant here. Higher-dimensional and higher-fidelity models of fluid transport can be explored in addition.

Implementation of the present design theory can be tailored to a chosen method of manufacturing IDFF channels. Here, linear conductance scaling to produce uniform flow (Eq. 4) imparts only one constraint to the geometry of a given channel's cross-section. For the micro-engraving process that we have used, varying only width or depth led to either an unresolved channel region of ~10% or an initial segment covering 50% of the entire channel length (Fig. S3), demonstrating the importance of sampling a wide range of cross-sections. Thus, additional constraints imposed by manufacturing can be included to produce different channel shapes than those that we have optimized for micro-engraving, subject nonetheless to the aforementioned conductance scaling. An experimental library of channel cross-sections whose hydraulic conductance is simulated can be created for other manufacturing methods to co-design tapered channels having piecewise-constant or continuously varying cross-sections. Laser micro-machining offers improved manufacturing scalability (see SI Sec. 13), but process optimization is needed to achieve the resolution and repeatability needed to accurately taper channels of the size tested here.

When implementing tapered channels in IDFFs that are embedded within porous electrodes, we have also shown that the spacing between channels can be impacted by the micro-environment occurring within electrode pores. Specifically, the hydrophobicity of binder likely causes a percolative path-length dependence of the hydraulic permeability within our porous electrodes. By choosing a small inter-channel distance for tapered-channel IDFFs, the hydraulic permeability between embedded channels was maximized while limiting material removal to 30%. Future efforts may address understanding how electrode formulation influences wettability and permeability, given that a scale-dependence of local electrode permeability was observed when a heated, neutral-pH coagulation bath was used for wet-phase inversion of electrodes.

Desalination experiments using symmetric FDI with tapered-channel IDFFs embedded in cation-intercalation electrodes showed significant reductions in energy use relative to straight-channel IDFFs. While both electrodes are effective in producing freshwater from seawater-salinity feeds, tapered-channel IDFFs did so with 62% lower pumping energy due to >2-fold increased hydraulic permeability: 2.5 kWh/m^3 compared to 6.6 kWh/m^3. Additionally tapered-channel IDFFs required 32% less overall energy than their straight-channel counterparts. This lower energy consumption of tapered-channel electrodes produced 2-fold and 1.3-fold increases in thermodynamic energy efficiency respectively at 50% and >95% salt removal from seawater salinity feeds. We also showed that the total energy consumption for brackish-salinity feeds can be reduced by 10 times compared to seawater salinity (0.69 kWh/m^3 compared to 7.3 kWh/m^3) by using optimally tapered IDFF channels. For brackish feeds tapered-channel IDFFs maximized thermodynamic energy efficiency at 82% salt removal to 31%, which exceeds the efficiency of conventional small-scale brackish desalination processes. Moreover most previous symmetric FDI studies focused on brackish desalination rather than seawater-salinity and achieved lower salt removal (<50%) [41,50–53] than we have demonstrated. Water recovery was also shown to be limited by water crossover rates through the intervening anion exchange membrane respectively at 0.11 L/m^2-h and 0.091 L/m^2-h for seawater- and brackish-salinity feeds. While these crossover rates are lower than for commercial ion-exchange membranes [57] in electrodialysis [58] and flow battery stacks [59] (0.24-2.5 L/m^2-h), reduction of water crossover could further increase water recovery and efficiency. We also note that the respective water productivities of 0.077 L/m^2-h and 2.3 L/m^2-h in the desalination of seawater- and brackish-salinity feeds is low in comparison to electrodialysis counterparts. Device and material optimization to increase operating current density could address this limitation.

4. Materials and methods

4.1. Synthesis of NiHCF Nanoparticles

Nickel hexacyanoferrate (NiHCF) nanoparticles were synthesized by a co-precipitation method outlined in our previous work [3,41]. Specifically, equal volume of 0.1 M $K_3Fe(CN)_6$ and 0.2 M $NiCl_2$ solutions were added dropwise into a beaker containing deionized water using two separate peristaltic pumps (NE-9000G, NewEra Pump System Inc.) at a flow rate of 1.5 mL/min under vigorous stirring. The resulting brown, yellow dispersion of NiHCF nanoparticles was sonicated for approximately 30 minutes and was allowed to settle down overnight. Afterwards, the nanoparticles were collected by centrifugation at 3900 rpm for 5 minutes. This process was repeated several times until the supernatant became clear before it was transferred to a petri dish to dry in an oven at 70°C overnight.

4.2. Electrode fabrication

Porous electrodes supported on graphite foil were fabricated using NiHCF nanoparticles, Ketjen black (KB) conductive additive (EC-600JB), and PVdF binder (Solvay Solef 5130) in an 80:5:15 mass ratio. The PVdF binder was dissolved in N-methyl-2-pyrrolidone (NMP, Sigma Aldrich) using a planetary mixer (Thinky, ARE-310) at 2000 rpm for 30 minutes to obtain a viscous solution of 50 mg/mL concentration. NiHCF nanoparticles and KB were finely ground in a vortex mill (Ultra Turra-X, IKA) using 18-20 steel balls (5.0 mm diameter) at 6000 rpm for 30 minutes. This powder mixture was combined with the PVdF solution in a ratio of 1 g of solid material per 3 mL of NMP using the planetary mixer at 2000 rpm for 30 minutes to obtain a homogeneous slurry. The slurry was then cast onto graphite foil (Ceramaterials) current collectors with 120 μm thickness using a doctor blade and a film applicator (Elcometer 4340) to produce wet electrode films of about 1.3 mm thick. These films were then solidified by wet phase inversion in a coagulation bath of deionized water heated to 85°C for 10-15 minutes. The electrodes were then dried in a fume hood for 2-3 hours before being placed in an electric oven at 70°C for about 12 hours. The uncalendared thickness of the dry electrodes, excluding graphite foil thickness, was measured to be 350 ± 50 μm. These electrodes were then calendared using a roll press (MTI-XTL) down to 200 ± 25 μm to reduce porosity and to enhance electrical conductivity before they were engraved with IDFFs over a 45 mm × 45 mm area using a desktop computer numerical control (CNC) machine. Electrode porosity and active material (NiHCF) loading were measured, as shown in Table 1.

4.3. Porosity and permeability measurement

The porosity ε of each porous electrode was determined as:

$$\varepsilon = 1 - \frac{\rho_f}{\rho_c}$$

where ρ_f is the electrode's film density and ρ_c is the mass-weighted density of the electrode's constituents:

Table 1
Electrode properties with tapered- and straight-channel IDFFs.

Channel type	NiHCF loading (mg/cm^2)	Porosity (%)		Permeability (μm^2)	
		Uncalendared	Calendared	k_{pe}	k_{app}
Tapered	19.1	60.5	32.6	0.35	70
	20.0	58.7	28.8	0.30	65
Straight	18.2	62.7	35.6	0.11	17
	17.5	64.8	37.9	0.15	32

$$\rho_c = \frac{1}{\left(\frac{\omega_{NiHCF}}{\rho_{NiHCF}} + \frac{\omega_{KB}}{\rho_{KB}} + \frac{\omega_{PVdF}}{\rho_{PVdF}}\right)}$$

where ω_{NiHCF}, ω_{KB}, and ω_{PVdF} are the mass fractions of NiHCF (0.8), KB (0.05), and PVdF (0.15), respectively. The densities of NiHCF ρ_{NiHCF}, KB ρ_{KB}, and PVdF ρ_{PVdF} were respectively estimated as 2.0 g/cc [62], 2.0 g/cc [63], and 1.75 g/cc [64].

The hydraulic permeability of each electrode was measured using a gravity-driven apparatus (Fig. S10). Here, a constant pressure head p was maintained, and Darcy's law was used to determine the permeability of the electrodes [3]:

$$k = \frac{\mu L_{e,\|} \dot{V}}{p A_c}$$

where μ is the dynamic viscosity of water (0.890 mPa-s) [65], $L_{e,\|}$ is the longitudinal length of the electrode, A_c is the superficial normal area of the electrode through which flow occurs, and $\dot{V}$ is the volumetric flow rate calculated as the ratio of the volume of water passed through the porous electrode to the elapsed time.

4.4. Micro-engraving of IDFFs into porous electrodes and library generation

IDFF channels were embedded into porous electrodes using a piecewise-constant conductance profile as described already. The toolpath for engraving these channels was determined using AutoCAD Fusion 360, and G-code was generated for execution on a desktop CNC machine. The machine was equipped with precision ball screws operated by closed-looped stepper motors controlled by GRBL Mega v.1.1 motion control fireware [66]. A V-bit engraving tool (Drill Bits Unlimited), featuring a 100 μm tip diameter and a 10° tip angle, was used for micro-engraving. A runout of about 80 μm was considered and compensated for due to the asymmetry of the tool bit. The electrode sample was secured on the CNC machine using a perforated aluminum plate (McMaster-Carr) mounted to a vacuum clamp (NEMI). 24,000 rev/min spindle speed was used with accompanying HEPA-filtered dust collection. The resulting channel cross-sections were characterized using optical profilometry (Keyence VK-X1000) showing a deviation from nominal dimensions within ± 5%. Representative cross-sections were determined by post-processing profilometry data after aligning each channel's axis in Cartesian space (SI Sec. 12). The corresponding channel conductance was simulated numerically based on a finite-volume scheme for two-dimensional variation of axial velocity $u_x(y,z)$ subject to incompressible, laminar, fully developed Poiseuille flow with no-slip boundaries:

$$\frac{\partial^2 u_x}{\partial y^2} + \frac{\partial^2 u_x}{\partial z^2} = -\frac{1}{\mu}\frac{dp}{dx}$$

4.5. Symmetric, intercalative FDI and desalination metrics

Two 250 μm thick graphite foil sheets were used for current collection in the symmetric, intercalation-based FDI flow cell (Fig. S11). IDFF-patterned 45 mm × 45 mm electrodes were then abutted to them as the cathode and anode, separated by a 150 μm thick anion-exchange membrane (Neosepta AMX). Before flow-cell assembly, one electrode was charged to obtain a 0% state-of-charge (SOC, 0.6 V vs. Ag/AgCl) in a flooded cell using a three-electrode setup, while the other was similarly fully discharged to obtain an SOC of 100% (0.1 V vs. Ag/AgCl). The flow-cell assembly was clamped using two 3D-printed end plates (Fig. S11). Two Z-type manifolds embedded within gasket material were used to supply diluate and brine to the respective electrodes. A VMP-3 multichannel potentiostat was used to supply 1 mA/cm^2 current in all desalination experiments, initially with 8 mL of diluate and 2 mL of

brine. Salt concentrations were measured using a 930 Compact Ion Chromatography system (Metrohm) while a Conduino system [67] was used to track the real-time concentrations of diluate and brine using calibrated conductance probes (Fig. 4 c; S6a,b).

Desalination performance metrics were determined as follows. The thermodynamic energy efficiency (TEE) was calculated as the ratio of the minimum specific energy consumption (SEC) to the cumulative SEC for each half-cycle. The SEC (kJ/mol) was determined using the electrical energy E_{elec} required to remove n_{salt} moles of salt per cycle.

$$SEC = \frac{E_{elec}}{n_{salt}} = \frac{\int_{t_0}^{t_{end}} I(t)V(t)dt}{n_{salt}}$$

where $I(t)$ and $V(t)$ are the applied current and cell potential as a function of time t. The minimum SEC was calculated as [3]:

$$(SEC)_{\min} = \frac{W_{rev}}{n_{salt}}$$

where W_{rev} is the amount of reversible work required for salt separation, determined using non-ideal activity coefficients:

$$W_{rev} = 2RT\left[V_D C_D \ln\left(f_{\pm}^{C_D} C_D\right) + V_B C_B \ln\left(f_{\pm}^{C_B} C_B\right) - (V_D + V_B) C_F \ln\left(f_{\pm}^{C_F} C_F\right)\right]$$

Here, V and C are volume and concentration with the subscripts D, B, and F being diluate, brine, and feed, respectively. The mean activity coefficient $f_{\pm}^{C_i}$ for any given salt concentration was obtained from literature [68]. The volumetric energy consumption (VEC) is the product of the specific energy consumption and the cumulative concentration of the salt removed.

The water-crossover rate (J_w) through the anion-exchange membrane was also calculated for each experiment as the ratio of the difference between initial (V_{D_0}) and final $\left(V_{D_f}\right)$ diluate volume to the product of the anion-exchange membrane area (A_{AEM}) and the elapsed time Δt [3]:

$$J_w = \frac{V_{D_0} - V_{D_f}}{A_{AEM}\Delta t}$$

CRediT authorship contribution statement

Md Habibur Rahman: Writing – review & editing, Writing – original draft, Methodology, Investigation, Formal analysis, Data curation. **Irwin C. Loud IV:** Writing – review & editing, Methodology, Investigation. **Vu Q. Do:** Writing – review & editing, Methodology, Investigation. **Md Abdul Hamid:** Writing – review & editing, Formal analysis. **Kyle C. Smith:** Writing – review & editing, Writing – original draft, Visualization, Supervision, Software, Resources, Project administration, Methodology, Investigation, Funding acquisition, Formal analysis, Conceptualization.

Declaration of competing interest

The authors declare the following financial interests/personal relationships which may be considered as potential competing interests:

Kyle C. Smith reports that financial support was provided by Office of Naval Research. Kyle C. Smith, Irwin C. Loud IV, and Vu Q. Do have patent #US Patent App. 17/980,017 pending. If there are other authors, they declare that they have no known competing financial interests or personal relationships that could have appeared to influence the work reported in this paper.

Acknowledgements

The Expeditionary Energy Program of the U.S. Office of Naval Research (Award No. N00014-22-1-2577) supported this research. Graduate student support from the department of Mechanical Science and Engineering at University of Illinois Urbana-Champaign (UIUC) is acknowledged. Optical profilometry was performed at the Materials Research Laboratory at UIUC. We thank Neil Pearse for supporting our access to the Trotec Speedy Flexx 400 laser at the Siebel Center for Design at UIUC.

Supplementary materials

Supplementary material associated with this article can be found, in the online version, at doi:10.1016/j.electacta.2024.145632.

Data availability

Data will be made available on request.

References

[1] M. Sauermoser, N. Kizilova, B.G. Pollet, S. Kjelstrup, Flow Field Patterns for Proton Exchange Membrane Fuel Cells, Front. Energy Res. 8 (2020) 482555, https://doi.org/10.3389/FENRG.2020.00013.
[2] X. Ke, J.M. Prahl, I.J.D. Alexander, J.S. Wainright, T.A. Zawodzinski, R.F. Savinell, Rechargeable redox flow batteries: flow fields, stacks and design considerations, Chem. Soc. Rev. 47 (2018) 8721–8743, https://doi.org/10.1039/C8CS00072G.
[3] V.Q. Do, E.R. Reale, I.C. Loud, P.G. Rozzi, H. Tan, D.A. Willis, K.C. Smith, Embedded, micro-interdigitated flow fields in high areal-loading intercalation electrodes towards seawater desalination and beyond, Energy Environ. Sci. 16 (2023) 3025–3039, https://doi.org/10.1039/D3EE01302B.
[4] R. Liu, Q. Zhang, Y. Shen, S. Yao, Optimization of flow field distribution to improve desalination performance of battery electrode deionization by designing flow channel structure, Sep. Purif. Technol. 331 (2024), https://doi.org/10.1016/j.seppur.2023.125661.
[5] H.M. Saif, T.H. Gebregeorgis, J.G. Crespo, S. Pawlowski, The influence of flow electrode channel design on flow capacitive deionization performance: experimental and CFD modelling insights, Desalination. 578 (2024) 117452, https://doi.org/10.1016/J.DESAL.2024.117452.
[6] R.M. Darling, M.L. Perry, The influence of electrode and channel configurations on flow battery performance, J. Electrochem. Soc. 161 (2014) A1381–A1387, https://doi.org/10.1149/2.0941409JES.
[7] D.S. Aaron, Q. Liu, Z. Tang, G.M. Grim, A.B. Papandrew, A. Turhan, T. A. Zawodzinski, M.M. Mench, Dramatic performance gains in vanadium redox flow batteries through modified cell architecture, J. Power. Sources. 206 (2012) 450–453, https://doi.org/10.1016/J.JPOWSOUR.2011.12.026.
[8] C.R. Dennison, E. Agar, B. Akuzum, E.C. Kumbur, Enhancing mass transport in redox flow batteries by tailoring flow field and electrode design, J. Electrochem. Soc. 163 (2016) A5163–A5169, https://doi.org/10.1149/2.0231601JES.
[9] S. Wan, H. Jiang, Z. Guo, C. He, X. Liang, N. Djilali, T. Zhao, Machine learning-assisted design of flow fields for redox flow batteries, Energy Environ. Sci. 15 (2022) 2874–2888, https://doi.org/10.1039/D1EE03224K.
[10] C.H. Lee, W.J.M. Kort-Kamp, H. Yu, D.A. Cullen, B.M. Patterson, T.A. Arman, S. Komini Babu, R. Mukundan, R.L. Borup, J.S. Spendelow, Grooved electrodes for high-power-density fuel cells, Nat. Energy 8 (2023) (2023) 685–694, https://doi.org/10.1038/s41560-023-01263-2.
[11] T.Y. Lin, S.E. Baker, E.B. Duoss, V.A. Beck, Topology optimization of 3D flow fields for flow batteries, J. Electrochem. Soc. 169 (2022) 050540, https://doi.org/10.1149/1945-7111/AC716D.
[12] L. Pan, J. Sun, H. Qi, M. Han, Q. Dai, J. Xu, S. Yao, Q. Li, L. Wei, T. Zhao, Dead-zone-compensated design as general method of flow field optimization for redox flow batteries, Proc. Natl. Acad. Sci. USA 120 (2023) e2305572120, https://doi.org/10.1073/PNAS.2305572120.
[13] X. Ke, J.M. Prahl, J.I.D. Alexander, R.F. Savinell, Redox flow batteries with serpentine flow fields: distributions of electrolyte flow reactant penetration into the porous carbon electrodes and effects on performance, J. Power. Sources. 384 (2018) 295–302, https://doi.org/10.1016/j.jpowsour.2018.03.001.
[14] A.A. Shah, H. Al-Fetlawi, F.C. Walsh, Dynamic modelling of hydrogen evolution effects in the all-vanadium redox flow battery, Electrochim. Acta 55 (2010) 1125–1139, https://doi.org/10.1016/j.electacta.2009.10.022.
[15] R. Schweiss, A. Pritzl, C. Meiser, Parasitic hydrogen evolution at different carbon fiber electrodes in vanadium redox flow batteries, J. Electrochem. Soc. 163 (2016) A2089–A2094, https://doi.org/10.1149/2.1281609jes.

[16] H. Al-Fetlawi, A.A. Shah, F.C. Walsh, Modelling the effects of oxygen evolution in the all-vanadium redox flow battery, Electrochim. Acta 55 (2010) 3192–3205, https://doi.org/10.1016/j.electacta.2009.12.085.
[17] M.D. Mat, K. Aldas, Application of a two-phase flow model for natural convection in an electrochemical cell, Int. J. Hydrogen. Energy 30 (2005) 411–420, https://doi.org/10.1016/j.ijhydene.2004.04.002.
[18] Y. Zeng, F. Li, F. Lu, X. Zhou, Y. Yuan, X. Cao, B. Xiang, A hierarchical interdigitated flow field design for scale-up of high-performance redox flow batteries, Appl. Energy 238 (2019) 435–441, https://doi.org/10.1016/j.apenergy.2019.01.107.
[19] N. Guo, M.C. Leu, U.O. Koylu, Bio-inspired flow field designs for polymer electrolyte membrane fuel cells, Int. J. Hydrogen. Energy 39 (2014) 21185–21195, https://doi.org/10.1016/J.IJHYDENE.2014.10.069.
[20] V. Muñoz-Perales, M. van der Heijden, P.A. García-Salaberri, M. Vera, A. Forner-Cuenca, Engineering lung-inspired flow field geometries for electrochemical flow cells with stereolithography 3D printing, ACS. Sustain. Chem. Eng. 11 (2023) 12243–12255, https://doi.org/10.1021/acssuschemeng.3c00848.
[21] D. Reed, E. Thomsen, B. Li, W. Wang, Z. Nie, B. Koeppel, V. Sprenkle, Performance of a low cost interdigitated flow design on a 1 kW class all vanadium mixed acid redox flow battery, J. Power. Sources. 306 (2016) 24–31, https://doi.org/10.1016/j.jpowsour.2015.11.089.
[22] Y. Xu, L. Peng, P. Yi, X. Lai, Analysis of the flow distribution for thin stamped bipolar plates with tapered channel shape, Int. J. Hydrogen. Energy 41 (2016) 5084–5095, https://doi.org/10.1016/J.IJHYDENE.2016.01.073.
[23] O.Lim Binyamin, Numerical investigation of tapered flow field configuration to improve mass transport and performance of proton exchange membrane fuel cell, Int. J. Hydrogen. Energy 50 (2024) 470–491, https://doi.org/10.1016/j.ijhydene.2023.08.247.
[24] M.R. Asadi, M. Ghasabehi, S. Ghanbari, M. Shams, The optimization of an innovative interdigitated flow field proton exchange membrane fuel cell by using artificial intelligence, Energy 290 (2024) 130131, https://doi.org/10.1016/J.ENERGY.2023.130131.
[25] K.M. Lisboa, J. Marschewski, N. Ebejer, P. Ruch, R.M. Cotta, B. Michel, D. Poulikakos, Mass transport enhancement in redox flow batteries with corrugated fluidic networks, J. Power. Sources. 359 (2017) 322–331, https://doi.org/10.1016/J.JPOWSOUR.2017.05.038.
[26] P.A. García-Salaberri, T.C. Gokoglan, S.E. Ibáñez, E. Agar, M. Vera, Modeling the effect of channel tapering on the pressure drop and flow distribution characteristics of interdigitated flow fields in redox flow batteries, Processes 8 (2020), https://doi.org/10.3390/PR8070775.
[27] C. Liu, L. Yin, Y. Lu, D. Alquier, Reactant gas transport and cell performance of proton exchange membrane fuel cells with tapered flow field design, J. Power. Sources. 158 (2006) 78–87, https://doi.org/10.1016/j.jpowsour.2005.09.017.
[28] E. Mancusi, É. Fontana, A.A. Ulson De Souza, S.M.A. Guelli Ulson De Souza, Numerical study of two-phase flow patterns in the gas channel of PEM fuel cells with tapered flow field design, Int. J. Hydrogen. Energy 39 (2014) 2261–2273, https://doi.org/10.1016/j.ijhydene.2013.11.106.
[29] Z. Zhang, S. Wu, H. Miao, T. Zhang, Numerical investigation of flow channel design and tapered slope effects on PEM fuel cell performance, Sustainability. 14 (2022) 1411167, https://doi.org/10.3390/SU141811167.
[30] E. Farokhi, M. Ghasabehi, M. Shams, Multi-objective optimization of a double tapered flow field proton exchange membrane fuel cell, Energy Rep. 10 (2023) 1652–1671, https://doi.org/10.1016/J.EGYR.2023.08.024.
[31] R.R. Kumar, S. Suresh, T. Suthakar, V.K. Singh, Experimental investigation on PEM fuel cell using serpentine with tapered flow channels, Int. J. Hydrogen. Energy 45 (2020) 15642–15649, https://doi.org/10.1016/j.ijhydene.2020.04.023.
[32] Y. Wang, X. Wang, Y. Fan, W. He, J. Guan, X. Wang, Numerical investigation of tapered flow field configurations for enhanced polymer electrolyte membrane fuel cell performance, Appl. Energy 306 (2022) 118021, https://doi.org/10.1016/j.apenergy.2021.118021.
[33] R. Liu, Y. Tian, Q. Zhang, Y. Shen, Enhanced Desalination performance of battery electrode deionization based on the optimized design of flow channel structure and channel section reconstruction, Ind. Eng. Chem. Res. 63 (2024) 13078–13089, https://doi.org/10.1021/acs.iecr.4c01284.
[34] P.A. Witherspoon, J.S.Y. Wang, K. Iwai, J.E. Gale, Validity of cubic law for fluid flow in a deformable rock fracture, Water. Resour. Res. 16 (1980) 1016–1024, https://doi.org/10.1029/WR016I006P01016.
[35] K.C. Smith, E.R. Reale, V.Q. Do, I.C. Loud, Flow channels for optimal or improved delivery of fluid to porous electrochemical /chemical media, US Patent App, 2022, 17/980,017.
[36] K.C. Smith, I.C. Loud, M.H. Rahman, C. Warden, V.Q. Do, A compact, low-pressure manifold with uniform flow at low Reynolds number, Physics of Fluids 36 (2024) 3295939, https://doi.org/10.1063/5.0211073.
[37] K.C. Smith, V.Q. Do, I.C. Loud, M.H. Rahman, C. Warden, Manifold design for uniform flow, 616, US Patent App, 2024, 18/743.
[38] P.A. Witherspoon, J.S.Y. Wang, K. Iwai, J.E. Gale, Validity of Cubic Law for fluid flow in a deformable rock fracture, Water. Resour. Res. 16 (1980) 1016–1024, https://doi.org/10.1029/WR016I006P01016.
[39] C. Hou, L. Du, Y. Li, M. Guo, J. Zhou, S. Qiao, Superhydrophobic PVDF membrane formed by crystallization process for direct contact membrane distillation, iScience 26 (2023) 106464, https://doi.org/10.1016/J.ISCI.2023.106464.
[40] S. Liang, Y. Kang, A. Tiraferri, E.P. Giannelis, X. Huang, M. Elimelech, Highly hydrophilic polyvinylidene fluoride (PVDF) ultrafiltration membranes via postfabrication grafting of surface-tailored silica nanoparticles, ACS. Appl. Mater. Interfaces. 5 (2013) 6694–6703, https://doi.org/10.1021/am401462e.
[41] E.R. Reale, L. Regenwetter, A. Agrawal, B. Dardón, N. Dicola, S. Sanagala, K. C. Smith, Low porosity, high areal-capacity Prussian blue analogue electrodes enhance salt removal and thermodynamic efficiency in symmetric Faradaic deionization with automated fluid control, Water. Res. X. (2021) 13, https://doi.org/10.1016/j.wroa.2021.100116.
[42] K.C. Smith, R. Dmello, Na-ion desalination (NID) enabled by Na-blocking membranes and symmetric Na-intercalation: porous-electrode modeling, J. Electrochem. Soc. 163 (2016) A530–A539, https://doi.org/10.1149/2.0761603JES.
[43] S. Liu, K.C. Smith, Quantifying the trade-offs between energy consumption and salt removal rate in membrane-free cation intercalation desalination, Electrochim. Acta 271 (2018) 652–665, https://doi.org/10.1016/J.ELECTACTA.2018.03.065.
[44] A. Shrivastava, V.Q. Do, K.C. Smith, Efficient, selective sodium and lithium removal by faradaic deionization using symmetric sodium titanium vanadium phosphate intercalation electrodes, ACS. Appl. Mater. Interfaces. 14 (2022) 30672–30682, https://doi.org/10.1021/ACSAMI.2C03261.
[45] W.E. Katz, The electrodialysis reversal (EDR) process, Desalination. 28 (1979) 31–40, https://doi.org/10.1016/S0011-9164(00)88124-2.
[46] L. Xu, W. Liu, X. Zhang, W. Tang, D.-J. Lee, Z. Yang, Z. Chen, S. Lin, Pseudo-continuous and scalable electrochemical ion pumping with circuit-switching-induced ion shuttling, Nature Water 2 (2024) (2024) 999–1008, https://doi.org/10.1038/s44221-024-00312-8.
[47] A. Al-Karaghouli, L.L. Kazmerski, Energy consumption and water production cost of conventional and renewable-energy-powered desalination processes, Renew. Sustain. Energy Rev. 24 (2013) 343–356, https://doi.org/10.1016/j.rser.2012.12.064.
[48] S.K. Patel, P.M. Biesheuvel, M. Elimelech, Energy Consumption of brackish water desalination: identifying the sweet spots for electrodialysis and reverse osmosis, ACS ES and T Engineering 1 (2021) 851–864, https://doi.org/10.1021/ACSESTENGG.0C00192.
[49] A. Ramachandran, D.I. Oyarzun, S.A. Hawks, M. Stadermann, J.G. Santiago, High water recovery and improved thermodynamic efficiency for capacitive deionization using variable flowrate operation, Water. Res. 155 (2019) 76–85, https://doi.org/10.1016/j.watres.2019.02.007.
[50] T. Kim, C.A. Gorski, B.E. Logan, Low energy desalination using battery electrode deionization, Environ. Sci. Technol. Lett. 4 (2017) 444–449, https://doi.org/10.1021/acs.estlett.7b00392.
[51] M. Son, V. Pothanamkandathil, W. Yang, J.S. Vrouwenvelder, C.A. Gorski, B. E. Logan, Improving the thermodynamic energy efficiency of battery electrode deionization using flow-through electrodes, Environ. Sci. Technol. 54 (2020) 3628–3635, https://doi.org/10.1021/acs.est.9b06843.
[52] E.R. Reale, A. Shrivastava, K.C. Smith, Effect of conductive additives on the transport properties of porous flow-through electrodes with insulative particles and their optimization for Faradaic deionization, Water. Res. 165 (2019) 114995, https://doi.org/10.1016/J.WATRES.2019.114995.
[53] V. Pothanamkandathil, J. Fortunato, C.A. Gorski, Electrochemical desalination using intercalating electrode materials: a comparison of energy demands, Environ. Sci. Technol. 54 (2020) 3653–3662, https://doi.org/10.1021/acs.est.9b07311.
[54] S. Porada, A. Shrivastava, P. Bukowska, P.M. Biesheuvel, K.C. Smith, Nickel hexacyanoferrate electrodes for continuous cation intercalation desalination of brackish water, Electrochim. Acta 255 (2017) 369–378, https://doi.org/10.1016/j.electacta.2017.09.137.
[55] J. Ahn, S. Kim, S. il Jeon, C. Lee, J. Lee, J. Yoon, Nafion-coated Prussian blue electrodes to enhance the stability and efficiency of battery desalination system, Desalination. 500 (2021) 114778, https://doi.org/10.1016/j.desal.2020.114778.
[56] R. Zhao, P.M. Biesheuvel, H. Miedema, H. Bruning, A. van der Wal, Charge efficiency: a functional tool to probe the double-layer structure inside of porous electrodes and application in the modeling of capacitive deionization, J. Phys. Chem. Lett. 1 (2010) 205–210, https://doi.org/10.1021/JZ900154H.
[57] R.S. Kingsbury, S. Zhu, S. Flotron, O. Coronell, Microstructure determines water and salt permeation in commercial ion-exchange membranes, ACS. Appl. Mater. Interfaces. 10 (2018) 39745–39756, https://doi.org/10.1021/ACSAMI.8B14494.
[58] H. Yan, Y. Wang, L. Wu, M.A. Shehzad, C. Jiang, R. Fu, Z. Liu, T. Xu, Multistage-batch electrodialysis to concentrate high-salinity solutions: Process optimisation, water transport, and energy consumption, J Memb Sci 570–571 (2019) 245–257, https://doi.org/10.1016/J.MEMSCI.2018.10.008.
[59] R.M. Darling, A.Z. Weber, M.C. Tucker, M.L. Perry, The influence of electric field on crossover in redox-flow batteries, J. Electrochem. Soc. 163 (2016) A5014–A5022, https://doi.org/10.1149/2.0031601JES.
[60] E.S. Beh, M.A. Benedict, D. Desai, J.B. Rivest, A redox-shuttled electrochemical method for energy-efficient separation of salt from water, ACS. Sustain. Chem. Eng. 7 (2019) 13411–13417, https://doi.org/10.1021/acssuschemeng.9b02720.
[61] G. Mohandass, W. Chen, S. Krishnan, T. Kim, Asymmetric and symmetric redox flow batteries for energy-efficient, high-recovery water desalination, Environ. Sci. Technol. 56 (2022) 4477–4488, https://doi.org/10.1021/ACS.EST.1C08609.
[62] S. Porada, A. Shrivastava, P. Bukowska, P.M. Biesheuvel, K.C. Smith, Nickel hexacyanoferrate electrodes for continuous cation intercalation desalination of brackish water, Electrochim. Acta 255 (2017) 369–378, https://doi.org/10.1016/j.electacta.2017.09.137.
[63] R.P. Rossman, W.R. Smith, Density of carbon black by helium displacement, Ind. Eng. Chem. 35 (2002) 972–976, https://doi.org/10.1021/IE50405A008.
[64] Solef ® PVDF Design & Processing Guide, 2015. chrome-extension://efaidnbmnnnibpcajpcglclefindmkaj/https://www.solvay.com/sites/g/files/srpend221/files/2018-08/Solef-PVDF-Design-and-Processing-Guide_EN-v2.7_0.pdf (accessed September 4, 2024).

[65] J. Kestin, M. Sokolov, W.A. Wakeham, Viscosity of liquid water in the range −8 °C to 150 °C, J. Phys. Chem. Ref. Data 7 (1978) 941–948, https://doi.org/10.1063/1.555581.
[66] GitHub - gnea/grbl-Mega: An open source, embedded, high performance g-code-parser and CNC milling controller written in optimized C that will run on an Arduino Mega2560, (2024). https://github.com/gnea/grbl-Mega (accessed March 21, 2024).
[67] M. Carminati, P. Luzzatto-Fegiz, Conduino: Affordable and high-resolution multichannel water conductivity sensor using micro USB connectors, Sens. Actuators. B Chem. 251 (2017) 1034–1041, https://doi.org/10.1016/J.SNB.2017.05.184.
[68] W.J. Hamer, Y. Yung chi, Osmotic Coefficients and Mean Activity Coefficients of Uni-univalent Electrolytes in Water at 25°C, J. Phys. Chem. Ref. Data 1 (1972) 1047–1100, https://doi.org/10.1063/1.3253108.